The Astrophysical Journal Letters, 926:L22 (9pp), 2022 February 20 https://doi.org/10.3847/2041-8213/ac52ac
© 2022. The Author(s). Published by the American Astronomical Society.
OPEN ACCESS

Deuterium Fractionation as a Multiphase Component Tracer in the Galactic Center

Laura Colzi[1,2], Jesús Martín-Pintado[1], Víctor M. Rivilla[1,2], Izaskun Jiménez-Serra[1], Shaoshan Zeng[3], Lucas F. Rodríguez-Almeida[1], Fernando Rico-Villas[1], Sergio Martín[4,5], and Miguel A. Requena-Torres[6,7]
[1] Centro de Astrobiología (CSIC-INTA), Ctra. de Ajalvir Km. 4, E-28850, Torrejón de Ardoz, Madrid, Spain; lcolzi@cab.inta-csic.es
[2] INAF-Osservatorio Astrofisico di Arcetri, Largo E. Fermi 5, I-50125, Florence, Italy
[3] Star and Planet Formation Laboratory, Cluster for Pioneering Research, RIKEN, 2–1 Hirosawa, Wako, Saitama, 351–0198, Japan
[4] European Southern Observatory, Alonso de Córdova, 3107, Vitacura, Santiago 763–0355, Chile
[5] Joint ALMA Observatory, Alonso de Córdova, 3107, Vitacura, Santiago 763–0355, Chile
[6] University of Maryland, College Park, MD 20742–2421, USA
[7] Department of Physics, Astronomy and Geosciences, Towson University, MD 21252, USA
Received 2021 December 9; revised 2022 January 31; accepted 2022 February 7; published 2022 February 21

Abstract

The Central Molecular Zone (CMZ) contains most of the mass of our Galaxy but its star formation rate is one order of magnitude lower than in the Galactic disk. This is likely related to the fact that the bulk of the gas in the CMZ is in a warm (>100 K) and turbulent phase with little material in the prestellar phase. We present in this Letter observations of deuterium fractionation (D/H ratios) of HCN, HNC, HCO^+, and N_2H^+ toward the CMZ molecular cloud G+0.693–0.027. These observations clearly show, for the first time, the presence of a colder, denser, and less turbulent narrow component, with a line width of ∼9 km s^{-1}, in addition to the warm, less dense, and turbulent broad component with a line width of ∼20 km s^{-1}. The very low D/H ratio $\leqslant 6 \times 10^{-5}$ for HCO^+ and N_2H^+, close to the cosmic value ($\sim 2.5 \times 10^{-5}$), and the high D/H ratios, $>4 \times 10^{-4}$ for HCN and HNC, derived for the broad component confirm the presence of high-temperature deuteration routes for nitriles. For the narrow component we have derived D/H ratios $>10^{-4}$ and excitation temperatures of 7 K for all molecules, suggesting kinetic temperatures $\leqslant$30 K and H_2 densities $\geqslant 5 \times 10^4$ cm^{-3}, at least one order of magnitude larger than that for the broad component. The method presented in this Letter allows us to identify clouds on the verge of star formation, i.e., under prestellar conditions, toward the CMZ. This method can also be used for the identification of such clouds in external galaxies.

Unified Astronomy Thesaurus concepts: Interstellar molecules (849); Isotopic abundances (867); Galactic center (565); Star formation (1569)

1. Introduction

The inner 500 pc of our Galaxy, known as the Central Molecular Zone (CMZ), contains ∼80% of the dense ($>10^4$ cm^{-3}) molecular gas in the Galaxy ($M_{CMZ} = 2$–6×10^7 $M_\odot$; Morris & Serabyn 1996). However, despite this large reservoir of matter, the star formation rate in the CMZ is at least one order of magnitude lower than that in the disk (Longmore et al. 2013; Barnes et al. 2017).

Even if this harsh environment is able to inhibit star formation, it does not stop it completely, and some star formation activity is taking place in the CMZ, as seen from the Arches and Quintuplet clusters and the younger protoclusters in the Sgr B2 region. The reasons for the suppression of star formation in the CMZ are still not fully understood but are related to its extreme environmental conditions that provide additional support against gravitational collapse (e.g., Morris & Serabyn 1996). In particular, the high level of turbulence due to the large internal cloud velocity dispersion (∼15–50 km s^{-1}; Morris & Serabyn 1996) and widespread high kinetic temperatures (T from ∼50 K to >100 K; Guesten & Ungerechts 1985; Huettemeister et al. 1993; Ginsburg et al. 2016; Krieger et al. 2017) could prevent star formation. In order to understand how star formation proceeds in the CMZ, it is crucial to identify and study the earlier evolutionary stages of the dense, cold, and quiescent prestellar cores. In principle, one expects that for prestellar cores to be formed, enough energy (turbulence) has to be dissipated so that gravitational collapse can proceed. Therefore, it is foreseen that prestellar cores in the CMZ also present narrower line emission than its surrounding turbulent gas. So far, only one progenitor of protoclusters in the CMZ has been proposed, the G0.253+0.016 molecular cloud, a.k.a. "the brick", which already shows all signposts of massive star formation (Longmore et al. 2012). However, it is still not clear whether the lack of detection of starless clouds at very early evolutionary stages is directly related to an observational bias. This is due to the presence of warm layers (or envelopes) with large column densities and high-velocity dispersion making it difficult to observationally disentangle the signatures of the denser and less turbulent prestellar gas.

The observation of deuterated molecules is a powerful tool to follow the history of the cold prestellar phase of star formation (Caselli & Ceccarelli 2012), both in low-mass and high-mass star-forming regions (e.g., Crapsi et al. 2005; Caselli et al. 2008; Emprechtinger et al. 2009; Fontani et al. 2011). The high densities ($n > 10^5$ cm^{-3}) and low temperatures ($T \leqslant 30$ K) of prestellar phases enhance the gas-phase abundance of H_3^+ because its main destroying agent, CO, depletes onto the surface of dust grains. The reaction of H_3^+ with HD (the main reservoir of D in the interstellar medium (ISM)) produces H_2D^+, which transfers D to other species. As a result, deuterium fractionation in molecules is known to increase their abundance by several orders of magnitude above the D primordial value, $D/H = (2.55 \pm 0.03) \times 10^{-5}$ (Zavarygin et al. 2018).

Original content from this work may be used under the terms of the Creative Commons Attribution 4.0 licence. Any further distribution of this work must maintain attribution to the author(s) and the title of the work, journal citation and DOI.

In this Letter, we illustrate how the deuterium fractionation of molecules (D/H ratio) traces the prestellar component embedded in massive warm and turbulent envelopes in the CMZ. We present observations of deuterated species of HCN, HNC, HCO^+, and N_2H^+ toward the warm and highly turbulent molecular cloud G+0.693−0.027 (hereafter G+0.693), located in the Sgr B2 complex. In particular, Sgr B2 consists of three main sources, Sgr B2(North), Sgr B2(Main), and Sgr B2(South), which are positioned along a north–south ridge. Because Sgr B2(N) is at an earlier stage of star formation than Sgr B2(M) (e.g., de Vicente et al. 2000), it seems the star formation activity occurs sequentially from the center to the north. If this is the case, early star formation activity is also expected toward G+0.693 because it is located ∼55″ northeast from Sgr B2(N). However, G+0.693 does not show any signposts of ongoing star formation such as ultracompact H II regions, H_2O masers, or dust continuum point sources (Ginsburg et al. 2018). A recent study of gas morphology and kinematics in this region (Zeng et al. 2020) suggests this cloud is affected by a cloud–cloud collision producing the shocks likely responsible for its rich chemistry due to the sputtering of molecules from dust grains (e.g., Requena-Torres et al. 2006; Martín et al. 2008; Zeng et al. 2018; Rivilla et al. 2019, 2020, 2021; Jiménez-Serra et al. 2020). In addition to the turbulent gas component (line widths $\geqslant$15–30 km s^{-1}), with a density of about 10^4 cm^{-3} and a gas temperature of >100 K (e.g., Zeng et al. 2018; Zeng et al. 2020), usually observed in the CMZ, the observed deuterated molecules pinpoint a new component with a denser ($n \geqslant 5\times10^4$ cm^{-3}), colder ($T\leqslant$ 30 K), and less turbulent (line widths ∼9 km s^{-1}) molecular gas component (prestellar) in the CMZ, which might be on the verge of gravitational collapse. Deuterated species can thus be used as key tracers to disentangle the multiphase components in the CMZ and reveal the location and physical conditions of cores where the next generation of stellar clusters will form.

2. Observations

The data presented in this work were taken from the high-sensitivity spectral survey toward the G+0.693 molecular cloud (e.g., Rodríguez-Almeida et al. 2021a, 2021b; Rivilla et al. 2021; Zeng et al. 2021) carried out with the IRAM 30m (Granada, Spain) and APEX (Chajnantor, Chile) radiotelescopes. The observations, centered at $\alpha_{J2000} = 17^h47^m22^s$ and $\delta_{J2000} = -28°21'27''$, were made in position-switching mode, with the off position located at (−885″, +290″) with respect to G+0.693.

The IRAM 30m observations were obtained during 2019 as part of projects 172–18 (PI Martín-Pintado), 018–19, and 133–19 (PI Rivilla). We have used the broadband Eight MIxer Receiver (EMIR) and FTS spectrometer (Fast Fourier Transform Spectrometer; Klein et al. 2012) to cover the frequency ranges 71.76–116.72 GHz, 124.77–175.5 GHz, 199.8−222.31 GHz, 223.32–238.29 GHz, 252.52−260.30 GHz, and 268.2−275.98 GHz, with a frequency resolution of ∼800 kHz, corresponding to 0.9–3.3 km s^{-1} at the observed frequencies. Pointing was checked every 1.5 hr, and focus was corrected at the beginning of the observations and after 4 hr. The half-power beamwidth (HPBW) of the telescope varies between 8.″9 and 34.″3 across the covered frequency range.

The APEX observations were obtained during 10 observing runs from 2021 July 11 to September 26 in service mode, for a total of 23.4 hr as part of project 0108.F-9308 (PI Rivilla). We used the NFLASH receiver, which allows the simultaneous observations of two sidebands, each one recorded by two spectrometer processors units (FFTS) of 4 GHz that overlap for 100 MHz, providing a total coverage of 7.9 GHz. We observed two different frequency setups centering the upper sideband at 262.0 GHz and 262.3 GHz, respectively. The covered spectral ranges were 243.94–252.12 GHz and 260.18–268.37 GHz, with a spectral resolution of 0.244 MHz (∼0.3 km s^{-1} at 262 GHz). The spectra analyzed in this work, which contain $H^{15}NC$(3–2) and $H^{13}C^{15}N$(3–2), have been smoothed to ∼800 kHz (∼1.1 km s^{-1} at 266 GHz) to match the spectral resolution of the IRAM 30m observations. The precipitable water vapor (pwv) during the observations was 0.7–3.6 mm. Focus was performed at the beginning of each observing run, and pointing was checked every 1–2 hr. The HPBW varies between 23.″2 and 25.″6 at the observed frequency range.

The line intensity of the spectra was measured in antenna temperature T_A^* units because the molecular emission toward G +0.693 is extended over the beam (e.g., Zeng et al. 2020).

3. Analysis and Results

We show the observed spectra of deuterated species of HCN, HNC, HCO^+, and N_2H^+ together with the optically thin isotopologues (^{13}C, ^{15}N, $^{13}C^{15}N$, and ^{18}O) of their hydrogen counterparts in Figures 1 and 2. Spectra of transitions blended with other species are shown in Figure A1. All the transitions targeted by our survey toward G+0.693 presented in this paper, which include the $J = 1$–0, $J = 2$–1, and $J = 3$–2 transitions, are summarized in Table B1.

Most the observed lines profiles cannot be fitted with a single Gaussian component. The low-lying energy transitions ($J = 1$–0 and $J = 2$–1) clearly show two components with different line widths (broad and narrow), except for those of DCO^+ and N_2D^+(2–1), and the $J = 3$–2 transitions of all molecules that mostly show the narrower component (see Figures 1 and 2). As we discuss in Section 4, the broad component belongs to the G+0.693 warm and turbulent gas (hereafter "broad" component), usually observed in the emission from transitions of most molecular species (e.g., Zeng et al. 2018; Rivilla et al. 2021). In contrast, the narrow component observed in the high-J lines and for DCO^+ and N_2D^+ reveals for the first time the presence of a less turbulent molecular gas (hereafter the "prestellar" component).

We have used the SLIM (Spectral Line Identification and Modeling) tool within the MADCUBA package[8] (Martín et al. 2019) to identify and perform the multi-line profile fitting. SLIM generates a synthetic spectrum, assuming local thermodynamic equilibrium (LTE) conditions, and applies an algorithm (AUTOFIT) to find the best nonlinear least-squares fit to the data. The free parameters to be fitted are the column density of the molecule, N, the excitation temperature, T_{ex}, the peak velocity, v_{LSR}, and the full width at half maxium (FWHM, see details in Martín et al. 2019).

To perform the LTE line fitting, we have only used the transitions that are not blended with emission from other species (see details in Table B1). The fit procedure requires a total of eight free parameters to take into account the two velocity components for each molecular species. Thus, to help the fit to converge we have fixed for all the species the T_{ex} and the FWHM to the values as explained below. To define the best FWHM for the narrow component, we have fitted a single

[8] Madrid Data Cube Analysis on ImageJ is a software developed at the Center of Astrobiology (CAB) in Madrid: https://cab.inta-csic.es/madcuba/.

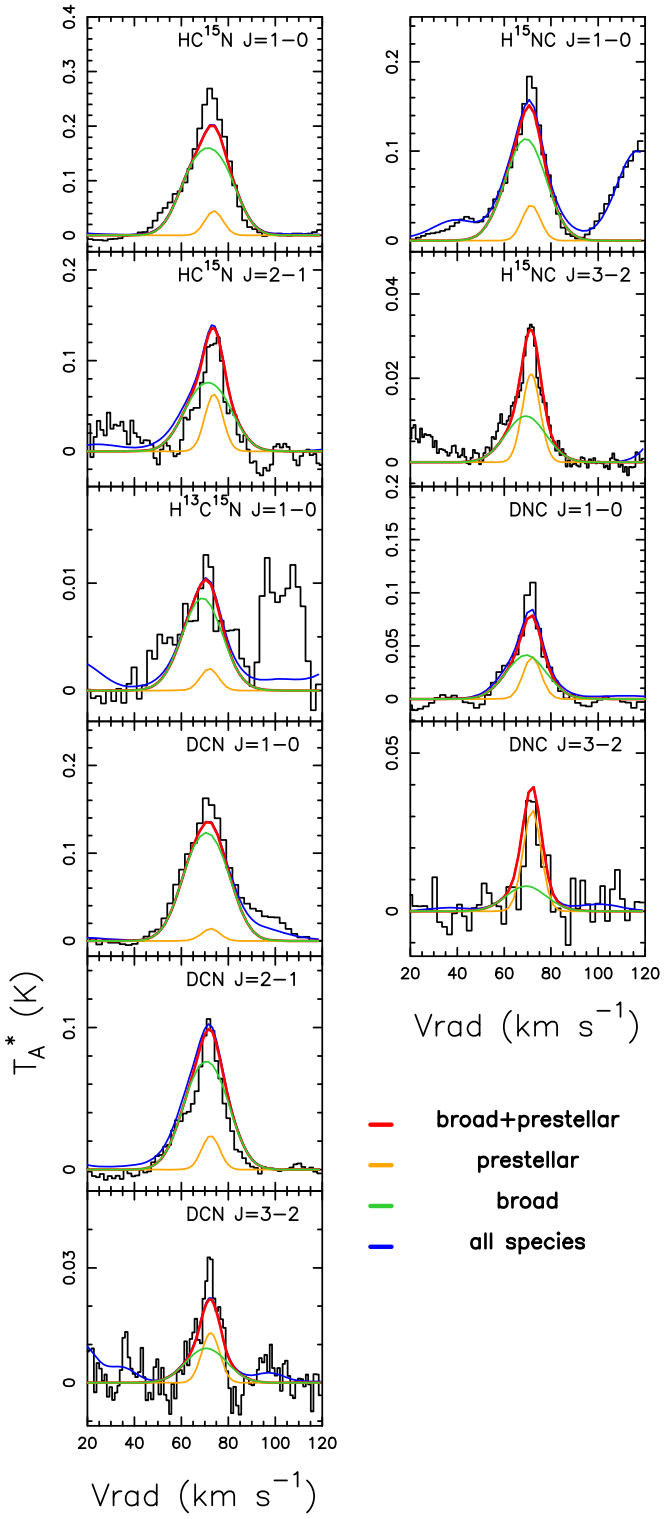

Figure 1. Observed transitions of the isotopologues of HCN (left) and HNC (right) studied in this work. The transition shown in each panel is indicated in the upper right. The orange line is the best LTE fit to the prestellar component, the green line is the best LTE fit to the broad gas component, and the red line is the sum of the components. The blue line indicates the total modeled line emission, including also the contribution of all molecular species previously identified in the survey (e.g., Rivilla et al. 2021; Rodríguez-Almeida et al. 2021a, 2021b; Zeng et al. 2021).

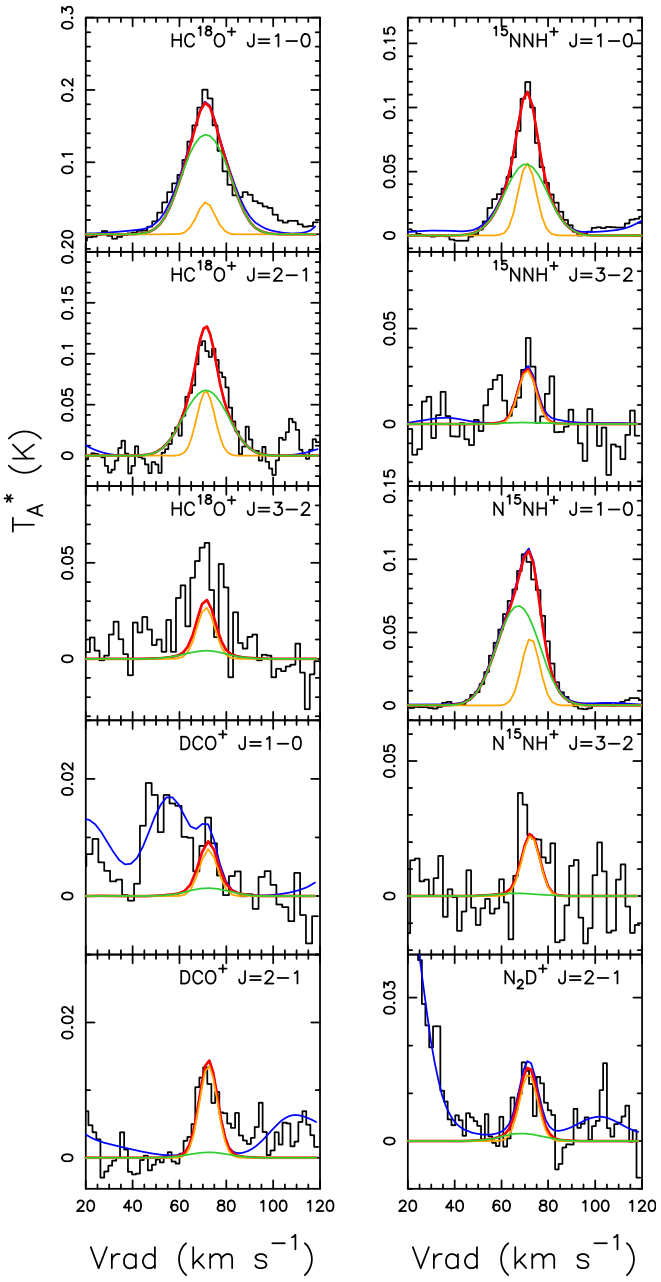

Figure 2. Observed transitions of the isotopologues of HCO^+ (left) and N_2H^+ (right) studied in this work. The transition shown in each panel is indicated in the upper right. The orange line is the best LTE fit to the prestellar component, the green line is the best LTE fit to the broad component, and the red line is the sum of the two profiles. The blue line indicates the total modeled line emission, including also the contribution of all molecular species previously identified in the survey (e.g., Rivilla et al. 2021; Rodríguez-Almeida et al. 2021a, 2021b; Zeng et al. 2021).

Gaussian profile to the transitions for which this component clearly dominates, i.e., $^{15}NNH^+$ and $N^{15}NH^+$(3–2), DNC(3–2), N_2D^+(2–1), and DCO^+(1–0) and (3–2). The average FWHM derived for these transition is 9 ± 2 km s^{-1}. Then, we have used the same procedure for the broad component using $HC^{18}O^+$(1–0), DCN(1–0), $H^{15}NC$(1–0), and $HC^{15}N$(1–0), obtaining an average FWHM of 20 ± 1 km s^{-1}. Thus, we have used for the broad and the prestellar components line widths of 20 km s^{-1} and 9 km s^{-1}, respectively, which reproduce well all the observed lines profiles for all molecules (Figures 1 and 2).

To derive the T_{ex}, we have used $HC^{18}O^+$ because it is the only non D-bearing species with three detected transitions ($J = 1$–0, 2–1, and 3–2) that appear unblended. The T_{ex} that

Table 1
Results from the LTE Fitting Procedure

Molecule	FWHM (km s^{-1})	v_{LSR} (km s^{-1})	T_{ex} (K)	N ($\times10^{12}$ cm^{-2})	D/H ($\times10^{-4}$)
			HCN		
DCN	9	72.5 ± 0.8	7	0.33 ± 0.06	
DCN	20	70.7 ± 0.3	3	39.8 ± 1.4	
$HC^{15}N$	9	73.9 ± 0.6	7	0.81 ± 0.15	4.5 ± 1.5
$HC^{15}N$	20	71.5 ± 0.6	3	51 ± 4	8.6 ± 1.9
$H^{13}C^{15}N$	9	72	7	0.072 ± 0.019	4 ± 2
$H^{13}C^{15}N$	20	69	3	1.4 ± 0.2	13 ± 4
			HNC		
DNC	9	71.9 ± 0.5	7	0.83 ± 0.11	
DNC	20	69.4 ± 1.1	4.3	2.4 ± 0.3	
$H^{15}NC$	9	71.55 ± 0.14	7	0.84 ± 0.04	11 ± 3
$H^{15}NC$	20	69.22 ± 0.16	4.3 ± 0.1	7.48 ± 0.16	3.6 ± 0.8
			HCO^+		
DCO^+	9	72.4 ± 0.5	7	0.12 ± 0.01	
DCO^+	20	70	3	⩽0.2[a]	
$HC^{18}O^+$	9	71.3 ± 0.6	7	0.48 ± 0.06	9 ± 2
$HC^{18}O^+$	20	71.3 ± 0.5	3	23.4 ± 1.5	⩽0.31
			N_2H^+		
N_2D^+	9	71.7 ± 0.8	7	0.15 ± 0.02	
N_2D^+	20	69	3	⩽0.5[b]	
$^{15}NNH^+$	9	71.01 ± 0.5	7	0.74 ± 0.09	2.2 ± 0.4
$^{15}NNH^+$	28	70.5 ± 0.9	3	8.9 ± 0.9	⩽0.64
$N^{15}NH^+$	9	72.5 ± 0.5	7	0.59 ± 0.09	2.7 ± 0.8
$N^{15}NH^+$	20	67.2 ± 0.7	3	11.2 ± 0.9	⩽0.51

Notes. Parameters without errors are fixed in the fitting procedure, as explained in Section 3.
[a] Upper limit derived taking into account the rms of ∼1.1 mK at 144.083 GHz.
[b] Upper limit derived taking into account the rms of ∼2.7 mK at 154.22 GHz.

better reproduce the three transitions (see left panel of Figure 2) are 7 K for the prestellar component and ∼3 K for the broad component. For $H^{15}NC$ we find that the broad component will be better fitted with T_{ex} of 4.3 ± 0.1 K. Given the possible uncertainties in the T_{ex} we used the values of 3 K and 7 K to fit the broad and prestellar components in other molecules, except for DNC for which we used the same T_{ex} derived from $H^{15}NC$. The difference in the T_{ex} clearly indicates that the prestellar component arises from higher-density gas than the broad component with $n \sim 10^4$ cm^{-3} (Zeng et al. 2020), but it only contributes 10% to the total column density. This will be discussed in Section 4.

We applied MADCUBA-AUTOFIT, leaving free N and v_{LSR}, with the exception of $H^{13}C^{15}N(3–2)$, for which the best fit to the line profiles were obtained with v_{LSR} fixed to 72 km s^{-1} and to 69 km s^{-1} for the prestellar and the broad components, respectively (see Table 1). The AUTOFIT provides the best solution for the free parameters, and their associated errors. The v_{LSR} obtained from the different molecules are consistent with a redshifted prestellar component with respect to the broad component. We are confident that this component is not associated with foreground gas because it would present a different velocity than the bulk of dense gas observed toward the star-forming regions in the Sgr B2 cloud (∼50–70 km s^{-1}; e.g., Goicoechea & Cernicharo 2002). We estimate that the total column density can be uncertain by up to 20% due to the absolute calibration errors.

The derived physical parameters are presented in Table 1, and the best LTE fits to the different line profiles are shown in Figures 1 and 2 with colored solid lines. The orange line corresponds to the prestellar component fit, the green line shows the fit to the broad component, and the red line is the sum of the two profiles. The additional blue line also shows the contribution from other molecular species previously identified in the survey (e.g., Zeng et al. 2018; Rivilla et al. 2021).

To compute the D/H ratios, the derived column density of the ^{13}C, ^{15}N, and ^{18}O isotopologues have been converted to the column densities of the main isotopologues using the typical isotopic ratios found in the CMZ: $^{12}C/^{13}C = 20$ (Wilson & Rood 1994), $^{14}N/^{15}N = 900$ (Guesten & Ungerechts 1985), or $^{16}O/^{18}O = 250$ (Wilson & Rood 1994). The quoted errors in the D/H ratios also consider an additional 20% error due to the assumed isotopic ratios. The D/H ratios obtained for HCN and HNC range from $\sim3.6 \times 10^{-4}$ up to $\sim1.3 \times 10^{-3}$, taking into account both components (see Table 1 and Figure 3). For HCO^+ and N_2H^+, the deuterated species were detected only in the prestellar component, giving D/H ratios $>10^{-4}$. For the broad component, in contrast, we derived upper limits for the

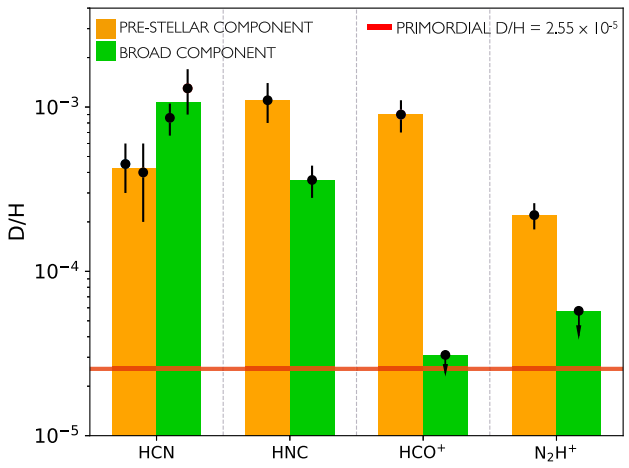

Figure 3. D/H ratios found for the different molecules, in the prestellar (orange) and broad (green) components. The red horizontal line indicates the primordial D/H value of $(2.55 \pm 0.03) \times 10^{-5}$ (Zavarygin et al. 2018).

D/H ratios $<3.1 \times 10^{-5}$ and $<5.7 \times 10^{-5}$ for HCO^+ and N_2H^+, respectively. The upper limits on the total column density of DCO^+ and N_2D^+ have been derived taking into account the 3σ rms of the integrated intensity at the rest frequencies indicated in Table 1. While the deuteration fraction between the prestellar and broad components are ∼0.4 and ∼3.3 for HCN and HNC, respectively, it increases to ⩾30 and ⩾4 for HCO^+ and N_2H^+, respectively. This clearly shows the large differences in the D fractionation for HCO^+ and N_2H^+ with respect to nitriles in both components.

We have also checked if the differences found in the isotopic compositions of the two components are still significant when considering different FWHM and T_{ex} than those used for the LTE fit. To do that, we have explored different values of these parameters for the two components and for which the fit converges. In particular, for the narrow component we have explored T_{ex} between 5 and 15 K, and for the broad component between 3 and 6 K. We have found that for the narrow component, the D/H ratios vary by factors of 1–1.8 and 1–3.4 with respect to those shown in Table 1 for HNC and N_2H^+, respectively, for the temperature ranges considered. For the broad component, the D/H ratio of HNC varies by factors of 0.9–1.3, and the D/H upper limit of N_2H^+ varies by factors of 0.4–1 with respect to those shown in Table 1. In the range of T_{ex} used, the deuteration fraction between the narrow and the broad components varies only between 3.3 and 4.3 for HNC and between >4 and >19 for N_2H^+. Thus, the differences in the isotopic composition of the two components and between the different species are still significant despite the possible uncertainties in T_{ex}.

We have also explored the effects of changes in the FWHM between 9 km s^{-1} and 11 km s^{-1} for the narrow component and between 15 km s^{-1} and 25 km s^{-1} for the broad component. In this case, for the narrow component, the D/H ratios vary by factors of 1–1.45 and 1–1.2 with respect to those shown in Table 1 for HNC and N_2H^+, respectively, for the FWHM ranges considered. For the broad component, the D/H ratio of HNC varies by factors of 1–1.14, and the D/H upper limit of N_2H^+ varies by factors of 1–1.25 with respect to those shown in Table 1. In the range of possible FWHMs, the deuteration fraction between the narrow and the broad component varies between 3.3 and 4 for HNC, and between >2 and >4 for N_2H^+. Thus, we conclude that the differences in the isotopic composition of the two components and for the two species are still significant even assuming rather extremes values of line widths and T_{ex}.

4. Discussion and Conclusions

The Sgr B2 cloud complex is one of the most active sites of star formation in our Galaxy. As already explained in Section 1, toward its densest part, this molecular cloud harbors three well-known massive star-forming clusters: Sgr B2(N) (in the north), Sgr B2(M) (in the center), and Sgr B2(S) (in the south) that comprise numerous compact and ultracompact H II regions (e.g., Gaume et al. 1995; Schmiedeke et al. 2016; Ginsburg et al. 2018). However, the presence of filament-, arc- and shell-shaped dense gas likely produced by stellar feedback (Martín-Pintado et al. 1999), and of a large population of high-mass protostellar cores found by Ginsburg et al. (2018), indicates that star formation is not restricted to the central cloud region, but it is also taking place in the extended envelope of Sgr B2. Because Sgr B2(M) is considered to be more evolved than Sgr B2(N) and (S) (e.g., de Vicente et al. 2000; Ginsburg et al. 2018), star-forming activity may proceed sequentially from Sgr B2(M) outwards, to continue toward Sgr B2(N) in the north and Sgr B2(S) in the south. In the scenario of sequential star formation, it is expected that G+0.693 is in an earlier evolutionary phase because it is located northeast of Sgr B2(N).

Previous observations toward the quiescent clouds in the GC traced only the turbulent warm gas in a very turbulent component unable to form stars. Our observations of deuterated species reveal, for the first time, very low D/H ratios in HCO^+ and N_2H^+, close to the cosmic value, for the turbulent broad component and the presence of a new narrow (FWHM of 9 km s^{-1}) quiescent component, with high levels of deuteration in HCN, HNC, HCO^+ and N_2H^+ ($D/H > 10^{-4}$; see Figure 3). This gas is clearly less turbulent (narrower FWHM) than the surrounding gas (broad gas component with a FWHM of 20 km s^{-1}), exhibiting properties similar to those found in Galactic disk prestellar cores. The different degrees of D fractionation found in HCO^+ and N_2H^+ for both components indicates that the prestellar component should have a kinetic temperature $T \leqslant 30$ K, smaller than the temperature of the broad component $T > 100$ K. Indeed, at low kinetic temperatures, the reaction (Dalgarno & Lepp 1984)

$$H_3^+ + HD \rightarrow H_2D^+ + H_2 + 232\ K \quad (1)$$

efficiently produces H_2D^+, which can react with N_2, CN, and CO, enhancing the abundances of N_2D^+, DCN, DNC, and DCO^+ to the observed values. The D/H ratios derived from HCN and HNC in both the broad and prestellar components are similar. This is in good agreement with the idea that DCN and DNC not only are formed at $T < 30$ K, as explained above, but also through additional high-temperature routes (see, e.g., Roueff et al. 2013). Indeed, for high temperatures ($T > 70$–80 K), the reaction

$$CH_3^+ + HD \rightarrow CH_2D^+ + H_2 + 654\ K \quad (2)$$

starts to be more efficient than reaction (1). Then, CH_2D^+ reacts with atomic N and initiates a chain of reactions that ends up with high deuterium fractionation in DCN and DNC ($D/H > 10^{-4}$; Roueff et al. 2007) and very low fractionation in N_2D^+ ($D/H < 3.1 \times 10^{-5}$), as observed for the broad warm

component. CH_2D^+, reacting with O and CO, could also contribute to an efficient formation of DCO^+ at high temperatures, as shown by Favre et al. (2015). However, these models show that these reactions are only efficient for the inner dense part of protoplanetary disks. Because we found for HCO^+ a very low D fractionation ($D/H < 3.1 \times 10^{-5}$) for the broad component, this suggests that such pathways are not efficient for the typical densities found in the GC ($\sim 10^4$ cm^{-3}).

The D/H values derived for the prestellar component toward G+0.693 are similar to previous observations of several deuterated complex organic molecules (COMs) toward the GC star-forming hot core Sgr B2(N2) (D/H from 5×10^{-4} to 4×10^{-3}; Belloche et al. 2016), of DCN toward the star-forming 50 km s^{-1} cloud in the Sgr A* region ($D/H = 4 \times 10^{-4}$, Lubowich et al. 2000), and of HDO toward Sgr B2 (D/H from 5×10^{-4} to 10^{-3}; Comito et al. 2003).

Previous measurements in the GC showed a much larger D/H ratio than the primordial value, indicating a large (20–200) degree of chemical fractionation. Jacq et al. (1999), Lubowich et al. (2000), and Polehampton et al. (2002) claimed, through chemical modeling, that the atomic D/H ratios may be up to $\sim$100 times lower in the Galactic center region than in the local ISM because of stellar processing in the interior of stars. Our measured upper limit of the D/H ratio, for the first time close to the cosmic D/H ratio, is still consistent with this claim, but the large differences in the degree of fractionation in different molecules suggest that model predictions need to be considered with caution. Further observations of DCO^+ and N_2D^+ toward other quiescent molecular clouds in the GC will firmly establish the degree of processing of the material in this region of the Galaxy.

Additional support for the presence of a multiphase ISM in the GC comes from the excitation temperature derived for both components in Table 1, which translate to very different H_2 densities. Using the non-LTE molecular radiative transfer model RADEX (van der Tak et al. 2007), we derive, for the warm broad component, assuming a kinetic temperature of 100 K and a FWHM of 20 km s^{-1}, that the derived T_{ex} of 3–4 K translate to H_2 densities of $0.3–3 \times 10^4$ cm^{-3}. For the cold prestellar component, assuming kinetic temperatures of 20–30 K and a FWHM of 9 km s^{-1}, with T_{ex} of 7 K, the required H_2 densities increase by at least one order of magnitude to $0.05–1 \times 10^6$ cm^{-3}. It should be noted that the densities obtained for the narrow component are a factor of 5 up to 30 larger than for the broad component of the molecular species studied in this work. This confirms that the two components are tracing different phases of molecular gas. Moreover, higher temperatures (e.g., 100 K) and lower densities (e.g., 10^4 cm^{-3}), similar to those of the broad component are not consistent either with the D/H ratios obtained or with the LTE and the non-LTE analysis performed for the narrow component as the predicted line intensities are one order of magnitude lower than observed. The large difference in the line width, the kinetic temperature, and the density from the warm broad component to the prestellar component suggests that a substantial fraction (10% in column density) of gas in the GC has the conditions to form the new generation of stars. This denser gas component was likely formed through the cloud–cloud collisions known to occur in the Sgr B2 complex (Fukui et al. 2021).

To conclude, in this Letter we have shown that combined observations of the degree of deuteration of different molecules, such as N_2H^+ and HCO^+, can be used to reveal the different gas components in the line of sight to the CMZ, allowing us to identify denser gas that is on the verge of gravitational collapse and that will host future protostars. A study of other similar sources in the CMZ could provide information on the ubiquity of the multiphase environment in the Galactic center. Moreover, the CMZ might be used as a template for the nuclei of other galaxies because some starburst galaxies like NGC 253, M82, and IC 342 contain gas with average densities and gas temperatures similar to those found in the CMZ for the broad warm component (e.g., Aladro et al. 2011). Thus, observations of deuterated molecules in nearby galaxies could be crucial to identify and investigate the earliest evolutionary stages of extragalactic protoclusters and to understand the full star formation sequence in external galaxies.

We thank the anonymous referee for the careful reading of the article and the useful comments. We are grateful to the IRAM 30 m telescope staff for their help during the different observing runs and to the APEX staff for conducting the observations. IRAM is supported by the National Institute for Universe Sciences and Astronomy/National Center for Scientific Research (France), Max Planck Society for the Advancement of Science (Germany), and the National Geographic Institute (IGN) (Spain). APEX is a collaboration between the Max-Planck-Institut fuer Radioastronomie, the European Southern Observatory, and the Onsala Observatory. L. C. and V. M.R. acknowledge support from the Comunidad de Madrid through the Atracción de Talento Investigador Senior Grant (COOL: Cosmic Origins Of Life; 2019-T1/TIC-15379). J.M.-P. and I.J.-S. have received partial support from the Spanish State Research Agency through project number PID2019-105552RB-C41.

Facilities: IRAM 30m, APEX.

Software: MADCUBA.

Appendix A
Blended Transitions

Figure A1 shows the transitions present in the spectral setup but not used for the analysis because they appear blended with other species.

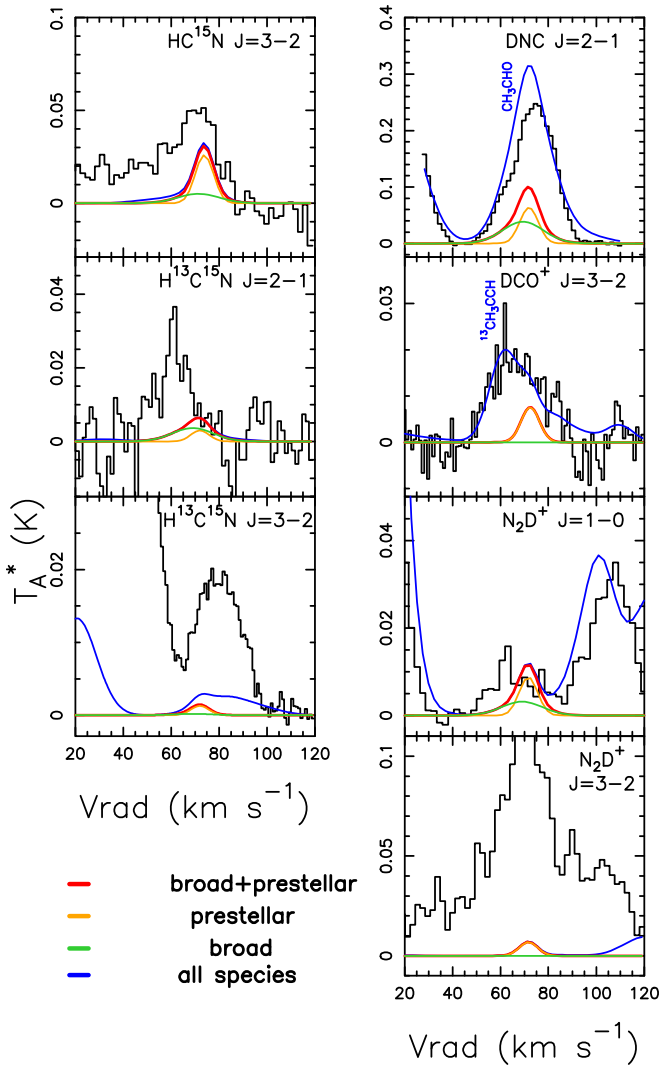

Figure A1. Observed transitions that are blended with other species. The molecule and transition shown in each panel are indicated in the upper right. Blending species are indicated in blue when known. The orange line is the best LTE fit to the prestellar component, the green line is the best LTE fit to the broad gas component, and the red line is the sum of the components. The blue line indicates the total modeled line emission, including also the contribution of all molecular species previously identified in the survey (e.g., Rodríguez-Almeida et al. 2021a, 2021b; Rivilla et al. 2021; Zeng et al. 2021).

Appendix B
Spectroscopic Information

The transitions of the molecules studied in this work were taken from the catalogs and spectroscopic works listed in Table B1. Moreover, Table B1 indicates possible blending with other species and the telescope used for the observation.

Table B1
Transitions of the Molecules Present in the G+0.693 Data Set (Section 2)

Molecule	Transition (J'–J)	Frequency (GHz)	log I (nm^2 MHz)	E_{up} (K)	Catalog/Entry/Date	Line List Reference	Dipole Moment Reference	Blended
$HC^{15}N$	1–0	86.0550	−2.5525	4.1	CDMS/28506/Dec. 2017	(1), (2)	(3)	No
$HC^{15}N$	2–1	172.1080	−1.6584	12.4	⋯	⋯	⋯	No
$HC^{15}N$	3–2	258.1570	−1.1450	24.8	⋯	⋯	⋯	Yes[a]
$H^{13}C^{15}N$	1–0	83.7276	−2.5875	4.0	CDMS/29512/Dec. 2006	(1)	(3)	No
$H^{13}C^{15}N$	2–1	167.4533	−1.6931	12.1	⋯	⋯	⋯	Yes[a]
$H^{13}C^{15}N$	3–2[b]	251.1752	−1.1794	24.1	⋯	⋯	⋯	Yes[a]
DCN	1–0	72.4147	−2.7990	3.5	CDMS/28509/Apr. 2006	(4), (5)	(6)	No
DCN	2–1	144.8280	−1.9034	10.4	⋯	⋯	⋯	No

Table B1
(Continued)

Molecule	Transition (J'–J)	Frequency (GHz)	log I (nm^2 MHz)	E_{up} (K)	Catalog/Entry/Date	Line List Reference	Dipole Moment Reference	Blended
DCN	3–2	217.2385	−1.3877	20.9	⋯	⋯	⋯	No
$H^{15}NC$	1–0	88.8657	−2.5690	4.3	JPL/28006/Dec. 1979	(7), (8)	(9)	No
$H^{15}NC$	3–2[b]	266.5878	−1.1624	25.6	⋯	⋯	⋯	No
DNC	1–0	76.3057	−2.6611	3.7	CDMS/28508/Sep. 2009	(10), (11), (12)	(9)	No
DNC	2–1	152.6097	−1.7660	11.0	⋯	⋯	⋯	Yes[c]
DNC	3–2	228.9105	−1.2510	22.0	⋯	⋯	⋯	No
$HC^{18}O^+$	1–0	85.1622	−2.3049	4.1	CDMS/31506/Dec. 2004	(13), (14)	(15)	No
$HC^{18}O^+$	2–1	170.3226	−1.4107	12.3	⋯	⋯	⋯	No
$HC^{18}O^+$	3–2	255.4794	−0.8972	24.5	⋯	⋯	⋯	No
DCO^+	1–0	72.0393	−2.5223	3.5	CDMS/30510/Sep. 2009	(10), (16), (17)	(15)	No
DCO^+	2–1	144.0773	−1.6267	10.4	⋯	⋯	⋯	No
DCO^+	3–2	216.1126	−1.1110	20.8	⋯	⋯	⋯	Yes[d]
$^{15}NNH^+$	1–0	90.2638	−2.3485	4.3	CDMS/30507/Mar. 2009	(18)	(19)	No
$^{15}NNH^+$	3–2	270.7836	−0.9422	26.0	⋯	⋯	⋯	No
$N^{15}NH^+$	1–0	91.2057	−2.3350	4.4	CDMS/30508/Mar. 2009	(18)	(19)	No
$N^{15}NH^+$	3–2	273.6090	−0.9290	26.3	⋯	⋯	⋯	No
N_2D^+	1–0	77.1092	−2.5531	3.7	CDMS/30509/Mar. 2009	(20), (21), (22)	(19)	Yes[a]
N_2D^+	2–1	154.2170	−1.6581	11.1	⋯	⋯	⋯	No
N_2D^+	3–2	231.3218	−1.1432	22.2	⋯	⋯	⋯	Yes[a]

Notes. The first column indicates the molecule for which the transitions are listed. The second and third columns show the rotational transitions and the related frequencies, respectively. log I is the base 10 logarithm of the integrated intensity at 300 K and E_{up} is the energy of the upper level. Columns 6–8 contain the spectroscopic information for the molecules studied in this work. The last column indicates whether the transition is blended or not with other molecular species. All the transitions have been observed with the IRAM 30m, except when specified with a note.
[a] Blended with an unidentified molecular species.
[b] Transition observed with APEX.
[c] Blended with CH_3CHO at 152.607 GHz.
[d] Blended with $^{13}CH_3CCH$ at 216.115 GHz and 216.119 GHz.
References. (1) Fuchs et al. (2004); (2) Cazzoli et al. (2005); (3) Ebenstein & Muenter (1984); (4) Brünken et al. (2004); (5) Möllmann et al. (2002); (6) DeLeon & Muenter (1984); (7) Creswell et al. (1976); (8) Pearson et al. (1976); (9) Blackman et al. (1976); (10) van der Tak et al. (2009); (11) Bechtel et al. (2006); (12) Okabayashi & Tanimoto (1993); (13) Plummer et al. (1983); (14) Schmid-Burgk et al. (2004); (15) Botschwina et al. (1993); (16) Caselli & Dore (2005); (17) Lattanzi et al. (2007); (18) Dore et al. (2009); (19) Havenith et al. (1990); (20) Pagani et al. (2009); (21) Dore et al. (2004); (22) Amano et al. (2005).

ORCID iDs

Laura Colzi https://orcid.org/0000-0001-8064-6394
Jesús Martín-Pintado https://orcid.org/0000-0003-4561-3508
Víctor M. Rivilla https://orcid.org/0000-0002-2887-5859
Izaskun Jiménez-Serra https://orcid.org/0000-0003-4493-8714
Lucas F. Rodríguez-Almeida https://orcid.org/0000-0002-9785-703X
Fernando Rico-Villas https://orcid.org/0000-0002-5351-3497
Sergio Martín https://orcid.org/0000-0001-9281-2919

References

Aladro, R., Martín-Pintado, J., Martín, S., Mauersberger, R., & Bayet, E. 2011, A&A, 525, A89
Amano, T., Hirao, T., & Takano, J. 2005, JMoSp, 234, 170
Barnes, A. T., Longmore, S. N., Battersby, C., et al. 2017, MNRAS, 469, 2263
Bechtel, H. A., Steeves, A. H., & Field, R. W. 2006, ApJL, 649, L53
Belloche, A., Müller, H. S. P., Garrod, R. T., & Menten, K. M. 2016, A&A, 587, A91
Blackman, G. L., Brown, R. D., Godfrey, P. D., & Gunn, H. I. 1976, Natur, 261, 395
Botschwina, P., Horn, M., Flügge, J., & Seeger, S. 1993, J. Chem. Soc., Faraday Trans., 89, 2219
Brünken, S., Fuchs, U., Lewen, F., et al. 2004, JMoSp, 225, 152
Caselli, P., & Dore, L. 2005, A&A, 433, 1145
Caselli, P., Vastel, C., Ceccarelli, C., et al. 2008, A&A, 492, 703
Cazzoli, G., Puzzarini, C., & Gauss, J. 2005, ApJS, 159, 181
Comito, C., Schilke, P., Gerin, M., et al. 2003, A&A, 402, 635
Crapsi, A., Caselli, P., Walmsley, C. M., et al. 2005, ApJ, 619, 379
Creswell, R. A., Pearson, E. F., Winnewisser, M., & Winnewisser, G. 1976, ZNatA, 31, 221
Dalgarno, A., & Lepp, S. 1984, ApJL, 287, L47
de Vicente, P., Martín-Pintado, J., Neri, R., & Colom, P. 2000, A&A, 361, 1058
DeLeon, R. L., & Muenter, J. S. 1984, JChPh, 80, 3992
Dore, L., Bizzocchi, L., Degli Esposti, C., & Tinti, F. 2009, A&A, 496, 275
Dore, L., Caselli, P., Beninati, S., et al. 2004, A&A, 413, 1177
Ebenstein, W. L., & Muenter, J. S. 1984, JChPh, 80, 3989
Emprechtinger, M., Caselli, P., Volgenau, N. H., Stutzki, J., & Wiedner, M. C. 2009, A&A, 493, 89
Favre, C., Bergin, E. A., Cleeves, L. I., et al. 2015, ApJL, 802, L23

Fontani, F., Palau, A., Caselli, P., et al. 2011, A&A, 529, L7
Fuchs, U., Bruenken, S., Fuchs, G. W., et al. 2004, ZNatA, 59, 861
Fukui, Y., Habe, A., Inoue, T., Enokiya, R., & Tachihara, K. 2021, PASJ, 73, S1
Gaume, R. A., Claussen, M. J., de Pree, C. G., Goss, W. M., & Mehringer, D. M. 1995, ApJ, 449, 663
Ginsburg, A., Bally, J., Barnes, A., et al. 2018, ApJ, 853, 171
Ginsburg, A., Henkel, C., Ao, Y., et al. 2016, A&A, 586, A50
Goicoechea, J. R., & Cernicharo, J. 2002, ApJL, 576, L77
Guesten, R., & Ungerechts, H. 1985, A&A, 145, 241
Havenith, M., Zwart, E., Leo Meerts, W., & Ter Meulen, J. J. 1990, JChPh, 93, 8446
Huettemeister, S., Wilson, T. L., Bania, T. M., & Martin-Pintado, J. 1993, A&A, 280, 255
Jacq, T., Baudry, A., Walmsley, C. M., & Caselli, P. 1999, A&A, 347, 957
Jiménez-Serra, I., Martín-Pintado, J., Rivilla, V. M., et al. 2020, AsBio, 20, 1048
Klein, B., Hochgürtel, S., Krämer, I., et al. 2012, A&A, 542, L3
Krieger, N., Ott, J., Beuther, H., et al. 2017, ApJ, 850, 77
Lattanzi, V., Walters, A., Drouin, B. J., & Pearson, J. C. 2007, ApJ, 662, 771
Longmore, S. N., Bally, J., Testi, L., et al. 2013, MNRAS, 429, 987
Longmore, S. N., Rathborne, J., Bastian, N., et al. 2012, ApJ, 746, 117
Lubowich, D. A., Pasachoff, J. M., Balonek, T. J., et al. 2000, Natur, 405, 1025
Martín, S., Martín-Pintado, J., Blanco-Sánchez, C., et al. 2019, A&A, 631, A159
Martín, S., Requena-Torres, M. A., Martín-Pintado, J., & Mauersberger, R. 2008, ApJ, 678, 245
Martín-Pintado, J., Gaume, R. A., Rodríguez-Fernández, N., de Vicente, P., & Wilson, T. L. 1999, ApJ, 519, 667
Möllmann, E., Maki, A. G., Winnewisser, M., Winnewisser, B. P., & Quapp, W. 2002, JMoSp, 212, 22
Morris, M., & Serabyn, E. 1996, ARA&A, 34, 645
Okabayashi, T., & Tanimoto, M. 1993, JChPh, 99, 3268
Pagani, L., Daniel, F., & Dubernet, M. L. 2009, A&A, 494, 719
Pearson, E. F., Creswell, R. A., Winnewisser, M., & Winnewisser, G. 1976, ZNatA, 31, 1394
Plummer, G. M., Herbst, E., & De Lucia, F. C. 1983, ApJL, 270, L99
Polehampton, E. T., Baluteau, J. P., Ceccarelli, C., Swinyard, B. M., & Caux, E. 2002, A&A, 388, L44
Requena-Torres, M. A., Martín-Pintado, J., Rodríguez-Franco, A., et al. 2006, A&A, 455, 971
Rivilla, V. M., Jiménez-Serra, I., Martín-Pintado, J., et al. 2021, PNAS, 118, e2101314118
Rivilla, V. M., Martín-Pintado, J., Jiménez-Serra, I., et al. 2019, MNRAS, 483, L114
Rivilla, V. M., Martín-Pintado, J., Jiménez-Serra, I., et al. 2020, ApJL, 899, L28
Rodríguez-Almeida, L. F., Jiménez-Serra, I., Rivilla, V. M., et al. 2021b, ApJL, 912, L11
Rodríguez-Almeida, L. F., Rivilla, V. M., Jiménez-Serra, I., et al. 2021a, A&A, 654, L1
Roueff, E., Gerin, M., Lis, D. C., et al. 2013, JPCA, 117, 9959
Roueff, E., Parise, B., & Herbst, E. 2007, A&A, 464, 245
Schmid-Burgk, J., Muders, D., Müller, H. S. P., & Brupbacher-Gatehouse, B. 2004, A&A, 419, 949
Schmiedeke, A., Schilke, P., Möller, T., et al. 2016, A&A, 588, A143
van der Tak, F. F. S., Black, J. H., Schöier, F. L., Jansen, D. J., & van Dishoeck, E. F. 2007, A&A, 468, 627
van der Tak, F. F. S., Müller, H. S. P., Harding, M. E., & Gauss, J. 2009, A&A, 507, 347
Wilson, T. L., & Rood, R. 1994, ARA&A, 32, 191
Zavarygin, E. O., Webb, J. K., Dumont, V., & Riemer-Sørensen, S. 2018, MNRAS, 477, 5536
Zeng, S., Jiménez-Serra, I., Rivilla, V. M., et al. 2018, MNRAS, 478, 2962
Zeng, S., Jiménez-Serra, I., Rivilla, V. M., et al. 2021, ApJL, 920, L27
Zeng, S., Zhang, Q., Jiménez-Serra, I., et al. 2020, MNRAS, 497, 4896